**S1. OH oxidation of benzene and toluene in the absence of $NO_x$**

Scheme S1 shows the major reaction channels for OH oxidation of benzene and toluene, as represented in the Master Chemical Mechanism (MCM) (http://mcm.leeds.ac.uk/MCMv3.3.1/) (Jenkin et al., 2003; Bloss et al., 2005). OH-initiated oxidation of light aromatics such as benzene and toluene occurs mainly via OH addition, with 90% preference (Calvert et al., 2002). The hydroxy-cyclohexadienyl radical so formed can react with $O_2$ to form a peroxy radical ($RO_2$), or can react with hydroperoxyl or peroxy radicals ($HO_2$ or $RO_2$) to form an alkoxy radical (RO). $RO_2$ radical formed from the former channel can undergo (Xu and Wang, 2013; Pan and Wang, 2014; Wu et al., 2014; Schwantes et al., 2017): 1) $O_2$ elimination and go back to the OH-addition adduct; 2) $HO_2$ elimination to form phenols; 3) cyclization to form bicyclic intermediate (a new alkyl radical); 4) intra-molecular H-shift; and 5) reactions with NO, $HO_2$, or $RO_2$ to form an alkoxy radical (RO). A number of studies have suggested that formation of phenols via the $HO_2$ elimination (pathways 2) and formation of the bicyclic intermediate through cyclization (pathway 3) are major fates of the $RO_2$ generated (Jenkin et al., 2003; Bloss et al., 2005; Wang et al., 2017), with pathway 2 occurs more rapidly than does pathway 3 (Schwantes et al., 2017). Reactions of the newly formed phenols (e.g., cresol from toluene) can again be initiated by OH radicals, which have rate constants one order of magnitude higher than those of the aromatic precursors (Calvert et al., 2002; Schwantes et al., 2017; Garmash et al., 2020). The bicyclic intermediate, on the other hand, is a new alkyl radical and can easily undergo $O_2$ addition to form a new $RO_2$ radical, analogous to the auto-oxidation of terpenoids or alkanes that forms highly oxygenated organic molecules (HOMs) (Crounse et al., 2013; Ehn et al., 2014; Berndt et al., 2016; Praske et al., 2018; Bianchi et al., 2019). This new $RO_2$ radical, which has an O-O bridge on a distorted aromatic ring and a (new) R-O-O group on one of the six carbons of the original ring, is termed as the bicyclic peroxy radical (BPR) (Calvert et al., 2002; Birdsall et al., 2010; Wu et al., 2014; Wang et al., 2017) and has been detected in experimental studies (Birdsall et al., 2010; Birdsall and Elrod, 2011; Zaytsev et al., 2019; Garmash et al., 2020).

**S2. Methods**

**Experimental setup**

In a typical experiment, the $O_3$ flow of 0.56 L min⁻¹, the humidified carrier gas flow of 3.3 L min⁻¹, and the $N_2O$ flow of 0.1 L min⁻¹ (only for high $NO_x$) were injected into the oxidation flow reactor (OFR). A small flow of benzene or toluene from gas cylinders was introduced into the OFR to achieve mixing ratios of 110 ppb for benzene and 50 ppb for toluene. The total flow was made up by dry zero air of about 4.3 L min⁻¹ to 8.4 L min⁻¹, resulting in an average residence time of 95 s. In the OFR, the voltage for the 254-nm lamp ballast (PAM lamp1) was set to sequentially step from 2 to 10 VDC to generate OH radicals with different concentrations. The voltage for the external ozone lamp ballast was maintained at 3.3 VDC, leading to an $O_3$ concentration of about 5 ppm at the exit of the OFR (OFR254-5). Figure S2 shows the experimental sequence of a typical OFR254-5 experiment for toluene. The flowrate for VOC injection was regularly set to zero for > 15 min, which we marked as "background" periods. After a full ramping of lamp voltage, the OFR was flushed with humidified zero air at full lamp power (i.e., all lamps at 10 VDC) for at least 4 hours for cleaning.

**Photochemical modeling**

We used an OFR-based photochemical box model (PAMchem) introduced by Lambe et al. (2017) to estimate the concentrations of reactive species (e.g., OH, $HO_2$, NO, and $NO_2$) in the OFR. The actinic flux at 254 nm ($I_{254}$) is a key parameter for the model. We conducted calibration experiments for $SO_2$ under low-$NO_x$ (no $N_2O$ addition; OFR254-5) and high-$NO_x$ (1.1% vol $N_2O$ addition; OFR254-5-i$N_2O$1.1) conditions to determine the $I_{254}$. $SO_2$ (5 ppm in $N_2$) in a gas cylinder was diluted

and injected to the OFR. The voltage of PAM lamp 1 was adjusted to achieve various OH exposure. The mixing ratio of $SO_2$ was measured at the exit of the OFR by a gas analyzer (Thermo, 43i). The integrated OH exposure was calculated from its relative decay. The relative light intensity was monitored by a photodiode in the OFR. We tuned $I_{254}$ in the model to best match the measured quantities. The final model results compared to the measurements are shown in Fig. S3. The model reproduces the measured decay of $SO_2$. The relationship between $I_{254}$ and measured irradiance is established. For benzene and toluene oxidation under various $NO_x$ conditions, $I_{254}$ ranged from 0.16 to $4.45 \times 10^{15}$ photon $cm^{-2}$ s. Derived steady-state OH exposure ranged from $1.1 \times 10^{11}$ to $2.5 \times 10^{12}$ molecules $cm^{-3}$ s, and $HO_2$ concentration was in the range of 0.5 to 2.4 ppb. The modeled concentrations of NO and $NO_2$ are listed in Table S1. Table S1 also summarizes other experimental conditions as well as the measured and derived quantities (Li et al., 2015; Peng et al., 2015; Lambe et al., 2017). According to Lambe et al. (2017), the uncertainty of the estimated OH exposure is about 25%, and those for other modeled quantities are 60%. Thus, the propagated uncertainties for $[NO_x]:[HO_2]$ ratios are about 104%.

**CIMS data analysis**

For the data measured by an Aerodyne time-of-flight chemical ionization mass spectrometer with nitrate as the ionization reagent ($NO_3^-$-TOF-CIMS), three principles were used for data analysis. First, to ensure that signals were truly from the reactions instead of contamination, positive matrix factorization (PMF) analysis was conducted on the unit mass resolution data between mass-to-charge ratio ($m/z$, in Th) 150 and 450 by using the Igor PMF evaluation tool (PET, version 3.04A). An example of the time series of identified PMF factors as well as experimental conditions is shown in Fig. S4. Factors that show greater signals during the "background" periods than the reaction periods were considered as non-production factors (background or contamination). The major ions in the spectra of those factors were removed from the final dataset prior to high-resolution fitting. Second, background signals of the oxygenated products were determined by the signals detected during the non-VOC periods. Third, although the formation of $NO_3^-$-adduct ions were preferable in our instrument settings of the $NO_3^-$-TOF-CIMS, the oxygenated products may be detected as adducts with $HNO_3NO_3^-$. This disturbed us when deciding the source of nitrogen atoms of formulas under high-$NO_x$ conditions. With high signals of the reagent ion $HNO_3HNO_3NO_3^-$ in our experiments, we expected that in the fitted ions with two or more nitrogen atoms, the nitrogen atoms were both from the reagent ions if there was a good correlation between the $NO_3^-$-adduct and $HNO_3NO_3^-$-adduct. As shown in Fig. S5a, the ion formula of $C_7H_8N_3O_9^-$ was assigned as $C_7H_7NO_3$-$HNO_3NO_3^-$ instead of $C_7H_8N_2O_6$-$NO_3^-$ because of the good correlation between the $NO_3^-$-adduct and $HNO_3NO_3^-$-adduct of $C_7H_7NO_3$. In Fig. S5b where a poor correlation was observed, the ion formula of $C_7H_{10}N_3O_{12}^-$ was assigned as $C_7H_{10}N_2O_9$-$NO_3^-$, and the two nitrogen atoms were perhaps originated from the gaseous oxygenated product itself. We also checked the isotope ratios to confirm the formulas, although the isotope signals were sometimes overridden by adjacent peaks. Only $NO_3^-$-adduct ions were presented in this study.

**S3. The RO pathway**

The formation of the even-oxygen open-shell products may involve RO pathways. In this pathway, the RO radical is formed from the reaction of $RO_2$ (with odd oxygen number) with $HO_2$ (or another $RO_2$), subtracting one oxygen atom from the $RO_2$ (R-S1). After that, the newly formed RO (with even oxygen number) isomerizes to a hydroxylated alkyl radical (R-S2) and results in a new $RO_2$ radical ($R'O_2$ with even oxygen number) via $O_2$ addition (R-S3) (Orlando et al., 2003).

$$C_xH_{y+1}O_{2n+1} (RO_2) + HO_2 \rightarrow C_xH_{y+1}O_{2n} (RO) + OH + O_2 \qquad \text{(R-S1)}$$

$$C_xH_{y+1}O_{2n} (RO) \rightarrow (HO)C_xH_yO_{2n-1} (R) \qquad \text{(R-S2)}$$

$$(HO)C_xH_yO_{2n-1} (R) + O_2 \rightarrow (HO)C_xH_yO_{2n+1} (i.e., C_xH_{y+1}O_{2n+2}, R'O_2) \qquad \text{(R-S3)}$$
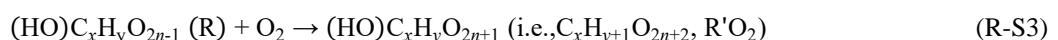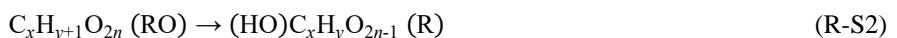
Formation of the closed-shell product $C_6H_6O_5$ in benzene oxidation might involve the RO pathway by the reaction between $C_6H_7O_5$ (BPR) and $HO_2$, forming $C_6H_7O_4$ (RO). Then H-shift (isomerization) and $O_2$ addition follows, and $C_6H_7O_4$ produces a new $RO_2$ radical with an even oxygen atom number ($C_6H_7O_6$). Xu et al. (2020) reported the formation of $C_6H_7O_6$ by the RO pathway of $C_6H_7O_4$. $C_6H_7O_6$ can be terminated by $HO_2$ or $RO_2$ to form the carbonyl of $C_6H_6O_5$.

## S4. Calculation of HOM molar yields

We follow the method described by Garmash et al. (2020) to calculate the molar yields of HOM products assuming their concentration has reached steady state at the exit of OFR. Some of the HOM products might not follow this assumption. The calculated molar yields are perhaps the lower. The formation rate of oxygenated products can be expressed as $k_1\gamma$[VOC][OH] (ppt s$^{-1}$), where $k_1$ (cm$^3$ molecule$^{-1}$ s$^{-1}$) is the VOC-OH reaction rate coefficient; $\gamma$ (dimensionless) is the fraction of the reaction producing oxygenated products that has been defined as the molar yield; [VOC] is the concentrations of the VOC precursors (ppt); [OH] is the concentrations of OH radicals (molecules cm$^{-3}$). The loss rate of HOMs, $k_{loss}$ (s$^{-1}$), includes the loss to the OFR walls ($k_{wall}$, s$^{-1}$), the loss to aerosol particles presented in the OFR (i.e., the condensation sink, CS, s$^{-1}$), and the loss to non-condensable products due to continuous reaction with OH ($k_{OHloss}$, s$^{-1}$) (Palm et al., 2016). For steady state, we have

$$\frac{d[\text{Oxygenated Products}]}{dt} = 0 \tag{S1}$$

Therefore, $k_1\gamma$[VOC][OH] $= k_{loss}$[HOMs]. The molar yield can be calculated as

$$\gamma = \frac{k_{loss}[\text{Oxygenated Products}]}{k_1[\text{VOC}][\text{OH}]} \tag{S2}$$

where

$$k_{loss} = k_{wall} + CS + k_{OHloss} \tag{S3}$$

We use $\tau_{wall}$, $\tau_{aer}$ and $\tau_{OHloss}$ to represent the characteristic times of HOMs for the loss to the OFR walls, to aerosol particles, and reaction with OH. The first-order loss rate of HOMs to the OFR walls is limited by eddy diffusion. Following the equation described by McMurry and Grosjean (1985), we have

$$k_{wall} = \frac{1}{\tau_{wall}} = \frac{A}{V} \cdot \frac{2}{\pi} \cdot \sqrt{k_e D_g} \tag{S4}$$

The OFR surface-area-to-volume ratio ($A/V$) is 25 m$^{-1}$. The coefficient of eddy diffusion ($k_e$) is 0.0042 s$^{-1}$, estimated by the method described by Brune (2019) and Huang et al. (2018). The molecular diffusion coefficient ($D_g$) is determined by the diffusion volume (i.e., 122) and the average molecular weight of HOMs (160 g mol$^{-1}$) for benzene and toluene oxidation, according to Kulmala et al. (1998) and Fuller et al. (1966). Eq. (S4) results in wall loss rate of 0.0028 s$^{-1}$, corresponding to $\tau_{wall}$ of 357 s, which is similar to the wall loss rate of 400-600 s estimated for OFR in previous studies (Lambe et al., 2011; Palm et al., 2016).

As described by Kulmala et al. (2012), the condensation sink can be calculated as follows:

$$CS = \frac{1}{\tau_{aer}} = 4\pi D_g \int_0^\infty r\, \beta(r) N(r) dr \tag{S5}$$

where $r$ is the radius of particle size bins, $N(r)$ is the particle number size distribution, and $\beta(r)$ is the correction factor for the transition regime. According to the Fuchs-Sutugin approximation, we have

$$\beta = \frac{1+k_n}{1+1.677k_n+1.333k_n^2} \tag{S6}$$

where $k_n$ is the Knudsen number that equals $\lambda_v/r$. $\lambda_v$ is the mean free path of vapor molecules that can be calculated as follows:

$$\lambda_v = 3D_g\sqrt{\frac{\pi m_x}{8kT}} \tag{S7}$$

where $m_x$ denotes the molecular weight of the oxygenated products and $k$ is the Boltzmann constant (Kulmala et al., 1998).

Palm et al. (2016) noted that in their high-CS case (OA concentrations > 1.5 µg m$^{-3}$), the condensation lifetime is shorter than 100 s (i.e., CS > 0.01 s$^{-1}$). And in a low-CS case (OA concentrations < 0.3 µg m$^{-3}$), the condensation lifetime is longer than 400 s (i.e., CS < 0.0025 s$^{-1}$), leading to significantly kinetically limited condensation (Palm et al., 2016; Peng and Jimenez, 2020). The average CS for the experiments herein is 0.07 ± 0.03 s$^{-1}$, indicating that condensation is an important fate of the HOMs for our experiments.

Finally, similar to the study of Palm et al. (2016), we estimated the continuous reaction loss of HOMs with OH as follows:

$$k_{\text{OHloss}} = \frac{1}{\tau_{\text{OHloss}}} \tag{S8}$$

$$\tau_{\text{OHloss}} = \frac{5}{k_{\text{OH}}[\text{OH}]} \tag{S9}$$

where we assume a rate constant for the reaction of HOMs with OH of $1.0 \times 10^{-11}$ cm$^3$ molecule$^{-1}$ s$^{-1}$ (Ziemann and Atkinson, 2012). Equations (S8) and (S9) result in an average $k_{\text{OHloss}}$ of 0.04 ± 0.02 s$^{-1}$.

**S5. Kinetic analysis**

**Formation of ROOH**

Under low-NO$_x$ conditions and low precursor concentrations (low RO$_2$), the termination of RO$_2$ proceeds mainly by HO$_2$ via reactions of R-S4 to R-S8 (Jenkin et al., 2019).

$$\text{RO}_2 + \text{HO}_2 \rightarrow \text{ROOH} + \text{O}_2 \tag{R-S4}$$

$$\text{RO}_2 + \text{HO}_2 \rightarrow \text{ROH} + \text{O}_3 \tag{R-S5}$$

$$\text{RO}_2 + \text{HO}_2 \rightarrow \text{R}_{\text{-H}}=\text{O} + \text{H}_2\text{O} + \text{O}_2 \tag{R-S6}$$

$$\text{RO}_2 + \text{HO}_2 \rightarrow \text{RO} + \text{OH} + \text{O}_2 \tag{R-S7}$$

$$\text{RO}_2 + \text{HO}_2 \rightarrow \text{R}_{\text{-H}}=\text{O} + \text{OH} + \text{HO}_2 \tag{R-S8}$$
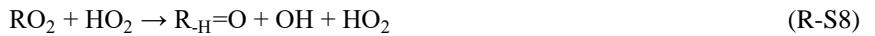
Jenkin et al. (2019) suggested that the overall rate coefficients of RO$_2$ + HO$_2$ for benzene and toluene oxidation are $1.92 \times 10^{-11}$ and $1.98 \times 10^{-11}$ cm$^3$ molecules$^{-1}$ s$^{-1}$ at 298 K, meaning a lifetime of about 1 - 5 s in our experiments. Our OFR experiments have a residence time of about 95 s, which is much longer than the RO$_2$ termination rate by HO$_2$. Thus, ROOH at the exit of the OFR can be assumed at steady state, meaning

$$\frac{\text{d[ROOH]}}{\text{dt}} = 0 \tag{S10}$$

Thus,

$$k_{\text{R-S4}}[\text{RO}_2][\text{HO}_2] = k_{\text{ROOH\_loss}}[\text{ROOH}] \tag{S11}$$

where $k_{\text{R-S4}}$ (cm$^3$ molecule$^{-1}$ s$^{-1}$) is the rate coefficient of Reaction R-S4, and $k_{\text{ROOH\_loss}}$ (s$^{-1}$) is the loss rate of ROOH. For the benzene-derived RO$_2$ radical of C$_6$H$_7$O$_7$, we have

$$k_{\text{R-S4}}[\text{C}_6\text{H}_7\text{O}_7][\text{HO}_2] = k_{\text{ROOH\_loss}}[\text{C}_6\text{H}_8\text{O}_7] \tag{S12}$$

$$k_{\text{R-S4}} = \frac{k_{\text{ROOH\_loss}}[\text{C}_6\text{H}_8\text{O}_7]}{[\text{HO}_2][\text{C}_6\text{H}_7\text{O}_7]} \tag{S13}$$

For the toluene-derived RO$_2$ radical of C$_7$H$_9$O$_7$, we have

$$k_{\text{R-S4}}[\text{C}_7\text{H}_9\text{O}_7][\text{HO}_2] = k_{\text{ROOH\_loss}}[\text{C}_7\text{H}_{10}\text{O}_7] \tag{S14}$$

$k_{\text{R-S4}}$ can therefore be constrained as follows:

$$k_{\text{R-S4}} = \frac{k_{\text{ROOH\_loss}}[\text{C}_7\text{H}_{10}\text{O}_7]}{[\text{HO}_2][\text{C}_7\text{H}_9\text{O}_7]} \tag{S15}$$

The concentrations of RO$_2$ radicals were detected by the NO$_3^-$-TOF-CIMS. [HO$_2$] were estimated by the PAMchem model. The $k_{\text{ROOH\_loss}}$ estimation were described in Sect S4. The slopes in Fig. 5a represent the rate coefficients of the hydroperoxide pathway, which are $1.20 \times 10^{-11}$ and $1.26 \times 10^{-11}$ cm$^3$ molecules$^{-1}$ s$^{-1}$. These rate coefficients indicate the branching ratios for

the hydroperoxide formation under low $NO_x$ conditions are 0.62 and 0.64 for benzene- and toluene-derived $RO_2$ ($C_xH_{y+1}O_7$), respectively, which are consistent with those found in literature (0.52 - 1.00) (Jenkin et al., 2019).

**Formation of RONO$_2$ and ROONO$_2$**

$$RO_2 + NO \rightarrow RO + NO_2 \tag{R-S9}$$

$$RO_2 + NO(+M) \rightarrow RONO_2(+M) \tag{R-S10}$$

$$RO_2 + NO_2 \rightleftharpoons ROONO_2 \tag{R-S11}$$

$$RC(O)OO + NO_2 \rightarrow RC(O)OONO_2 \tag{R-S12}$$

The fraction of the reaction proceeding via the terminating channel R-S10 for a specific peroxy radical can be calculated as follows:

$$R_{\text{R-S10}} = k_{\text{R-S10}}/(k_{\text{R-S9}}+k_{\text{R-S10}}) = f_a f_b(R°/(1+R°)) \tag{S16}$$

where R° can be calculated on the basis of temperature and the molecular formula of the peroxy radical. The scaling factors, $f_a$ and $f_b$, are used to allow for systematic variations in the yields of RONO$_2$ for primary, secondary and tertiary radicals ($f_a$), and for the presence of oxygenated functional groups ($f_b$) (Jenkin et al., 2019). For forming hydroxy-dioxa-bicyclo peroxy radical ($C_6H_7O_5$) in benzene oxidation, R° is 0.3722, and $f_a$ and $f_b$ are 1.0 and 0.33, respectively. Thus, $R_{\text{R-S10}}$ for $C_6H_7O_5$ is 0.0895. For forming the hydroxy-dioxa-bicyclo peroxy radical ($C_7H_9O_5$) in toluene oxidation, R° is 0.3951, and $f_a$ and $f_b$ are 1.0 and 0.33, 0.43 and 0.33, or 0.13 and 0.33, respectively, depending on the position of the substituted groups. Thus, the $R_{\text{R-S10}}$ for $C_7H_9O_5$ is 0.0935, 0.0402, or 0.0122. Jenkin et al. (2019) suggest a generic rate coefficient of $RO_2$ + NO at 298 K of $9.04 \times 10^{-12}$ cm$^3$ molecules$^{-1}$ s$^{-1}$. Based on the rate coefficient and the branching ratios above for $C_xH_{y+1}O_5$, the formation rate coefficients of RONO$_2$ ($k_{\text{R-S10}}$) for the $RO_2$ radicals of $C_xH_{y+1}O_7$ in our experiments are estimated to be $8.09 \times 10^{-13}$ and $1.10 - 8.45 \times 10^{-13}$ cm$^3$ molecules$^{-1}$ s$^{-1}$, respectively. Similar to ROOH, RONO$_2$ at the exit of the OFR can be assumed at steady state, meaning

$$\frac{d[RONO_2]}{dt} = 0 \tag{S17}$$

$$k_{\text{R-S10}}[RO_2][NO] = k_{\text{RONO}_2\text{\_loss}}[RONO_2] \tag{S18}$$

where $k_{\text{RONO}_2\text{\_loss}}$ (s$^{-1}$) is the loss rate of the RONO$_2$. We then have

$$\frac{[RONO_2]}{[ROOH]} = \frac{k_{\text{R-S10}}}{k_{\text{R-S4}}} \times \frac{k_{\text{ROOH\_loss}}}{k_{\text{RONO}_2\text{\_loss}}} \times \frac{[NO]}{[HO_2]} \tag{S19}$$

$k_{\text{ROOH\_loss}}$ and $k_{\text{RONO}_2\text{\_loss}}$ are expectedly similar because of similar molecular weights and oxygen contents for ROOH and RONO$_2$ in the same experiment. Therefore, we have:

$$\frac{[RONO_2]}{[ROOH]} = \frac{k_{\text{R-S10}}}{k_{\text{R-S4}}} \times \frac{[NO]}{[HO_2]} \tag{S20}$$

For the benzene-derived $RO_2$ radical $C_6H_7O_7$, we have

$$\frac{[C_6H_7NO_8]}{[C_6H_8O_7]} = \frac{k_{\text{R-S10}}}{k_{\text{R-S4}}} \times \frac{[NO]}{[HO_2]} \tag{S21}$$

For the toluene-derived $RO_2$ radical $C_7H_9O_7$, we have

$$\frac{[C_7H_9NO_8]}{[C_7H_{10}O_7]} = \frac{k_{\text{R-S10}}}{k_{\text{R-S4}}} \times \frac{[NO]}{[HO_2]} \tag{S22}$$

Here, the concentrations of HOMs were detected by $NO_3^-$-TOF-CIMS. [NO] and [HO$_2$] were estimated by the PAMchem model. Similar to the analysis of the ROOH formation, the slopes in Fig. 5b suggest that the formation rate coefficients of RONO$_2$ are $2.87 \times 10^{-11}$ and $6.12 \times 10^{-11}$ cm$^3$ molecules$^{-1}$ s$^{-1}$ for benzene and toluene oxidation under our OFR254-5-iN$_2$O1.1 conditions, respectively. These coefficients are more than one order of magnitude greater than the values estimated above from the literature (i.e., $8.09 \times 10^{-13}$ and $1.10 - 8.45 \times 10^{-13}$ cm$^3$ molecules$^{-1}$ s$^{-1}$ for benzene and toluene oxidation, respectively) (Jenkin et al., 2019).

# References

Berndt, T., Richters, S., Jokinen, T., Hyttinen, N., Kurten, T., Otkjaer, R. V., Kjaergaard, H. G., Stratmann, F., Herrmann, H.,
190    Sipila, M., Kulmala, M., and Ehn, M.: Hydroxyl radical-induced formation of highly oxidized organic compounds, Nat.
       Commun., 7, 13677, https://doi.org/10.1038/ncomms13677, 2016.

Bianchi, F., Kurten, T., Riva, M., Mohr, C., Rissanen, M. P., Roldin, P., Berndt, T., Crounse, J. D., Wennberg, P. O., Mentel,
       T. F., Wildt, J., Junninen, H., Jokinen, T., Kulmala, M., Worsnop, D. R., Thornton, J. A., Donahue, N., Kjaergaard, H. G.,
       and Ehn, M.: Highly oxygenated organic oolecules (HOM) from gas-phase autoxidation involving peroxy radicals: a key
195    contributor to atmospheric aerosol, Chem. Rev., 119, 3472-3509, https://doi.org/10.1021/acs.chemrev.8b00395, 2019.

Birdsall, A. W., Andreoni, J. F., and Elrod, M. J.: Investigation of the role of bicyclic peroxy radicals in the oxidation
       mechanism of toluene, J. Phys. Chem. A, 114, 10655-10663, https://doi.org/10.1021/jp105467e, 2010.

Birdsall, A. W., and Elrod, M. J.: Comprehensive NO-dependent study of the products of the oxidation of atmospherically
       relevant aromatic compounds, J. Phys. Chem. A, 115, 5397-5407, https://doi.org/10.1021/jp2010327, 2011.

200    Bloss, C., Wagner, V., Jenkin, M. E., Volkamer, R., Bloss, W. J., Lee, J. D., Heard, D. E., Wirtz, K., Martin-Reviejo, M., Rea,
       G., Wenger, J. C., and Pilling, M. J.: Development of a detailed chemical mechanism (MCMv3.1) for the atmospheric
       oxidation of aromatic hydrocarbons, Atmos. Chem. Phys., 5, 641-664, https://doi.org/10.5194/acp-5-641-2005, 2005.

Brune, W. H.: The chamber wall index for gas-wall interactions in atmospheric environmental enclosures, Environ. Sci.
       Technol., 53, 3645-3652, https://doi.org/10.1021/acs.est.8b06260, 2019.

205    Calvert, J. G., Atkinson, R., Becker, K. H., Kamens, R. M., Seinfeld, J. H., Wallington, T. J., and Yarwood, G. Y.: The
       mechanisms of atmospheric oxidation of aromatic hydrocarbons, Oxford University Press, New York, 2002.

Crounse, J. D., Nielsen, L. B., Jørgensen, S., Kjaergaard, H. G., and Wennberg, P. O.: Autoxidation of organic compounds in
       the atmosphere, J. Phys. Chem. Lett., 4, 3513-3520, https://doi.org/10.1021/jz4019207, 2013.

Ehn, M., Thornton, J. A., Kleist, E., Sipila, M., Junninen, H., Pullinen, I., Springer, M., Rubach, F., Tillmann, R., Lee, B.,
210    Lopez-Hilfiker, F., Andres, S., Acir, I. H., Rissanen, M., Jokinen, T., Schobesberger, S., Kangasluoma, J., Kontkanen, J.,
       Nieminen, T., Kurten, T., Nielsen, L. B., Jorgensen, S., Kjaergaard, H. G., Canagaratna, M., Dal Maso, M., Berndt, T.,
       Petaja, T., Wahner, A., Kerminen, V. M., Kulmala, M., Worsnop, D. R., Wildt, J., and Mentel, T. F.: A large source of low-
       volatility secondary organic aerosol, Nature, 506, 476-479, https://doi.org/10.1038/nature13032, 2014.

Fuller, E. N., Schettler, P. D., and Giddings, J. C.: A new method for prediction of binary gas-phase diffusion coefficients, Ind.
215    Eng. Chem., 58, 18-27, https://doi.org/10.1021/ie50677a007, 1966.

Garmash, O., Rissanen, M. P., Pullinen, I., Schmitt, S., Kausiala, O., Tillmann, R., Zhao, D., Percival, C., Bannan, T. J.,
       Priestley, M., Hallquist, Å. M., Kleist, E., Kiendler-Scharr, A., Hallquist, M., Berndt, T., McFiggans, G., Wildt, J., Mentel,
       T. F., and Ehn, M.: Multi-generation OH oxidation as a source for highly oxygenated organic molecules from aromatics,
       Atmos. Chem. Phys., 20, 515-537, https://doi.org/10.5194/acp-20-515-2020, 2020.

220    Huang, M. Q., Lin, Y. H., Huang, X. Y., Liu, X. Q., Hu, C. J., Gu, X. J., Zhao, W. X., Fang, L., and Zhang, W. J.: Chemical
       analysis of aged benzene secondary organic aerosol using aerosol laser time-of-flight mass spectrometer, J. Atmos. Chem.,
       71, 213-224, https://doi.org/10.1007/s10874-014-9291-z, 2014.

Huang, Y. L., Zhao, R., Charan, S. M., Kenseth, C. M., Zhang, X., and Seinfeld, J. H.: Unified Theory of Vapor-Wall Mass
       Transport in Teflon-Walled Environmental Chambers, Environ. Sci. Technol., 52, 2134-2142,
225    https://doi.org/10.1021/acs.est.7b05575, 2018.

Jenkin, M. E., Saunders, S. M., Wagner, V., and Pilling, M. J.: Protocol for the development of the Master Chemical
       Mechanism, MCM v3 (Part B): tropospheric degradation of aromatic volatile organic compounds, Atmos. Chem. Phys., 3,
       181-193, https://doi.org/10.5194/acp-3-181-2003, 2003.

Jenkin, M. E., Valorso, R., Aumont, B., and Rickard, A. R.: Estimation of rate coefficients and branching ratios for reactions

230       of organic peroxy radicals for use in automated mechanism construction, Atmos. Chem. Phys., 19, 7691-7717, https://doi.org/10.5194/acp-19-7691-2019, 2019.

Kulmala, M., Toivonen, A., Mäkelä, J. M., and Laaksonen, A.: Analysis of the growth of nucleation mode particles observed in Boreal forest, Tellus B, 50, 449-462, https://doi.org/10.3402/tellusb.v50i5.16229, 1998.

Kulmala, M., Petäjä, T., Nieminen, T., Sipilä, M., Manninen, H. E., Lehtipalo, K., Dal Maso, M., Aalto, P. P., Junninen, H.,
235       Paasonen, P., Riipinen, I., Lehtinen, K. E. J., Laaksonen, A., and Kerminen, V.-M.: Measurement of the nucleation of atmospheric aerosol particles, Nat. Protoc., 7, 1651-1667, https://doi.org/10.1038/nprot.2012.091, 2012.

Lambe, A., Massoli, P., Zhang, X., Canagaratna, M., Nowak, J., Daube, C., Yan, C., Nie, W., Onasch, T., Jayne, J., Kolb, C., Davidovits, P., Worsnop, D., and Brune, W.: Controlled nitric oxide production via O(1-D) + N2O reactions for use in oxidation flow reactor studies, Atmos. Meas. Tech., 10, 2283-2298, https://doi.org/10.5194/amt-10-2283-2017, 2017.

240       Lambe, A. T., Ahern, A. T., Williams, L. R., Slowik, J. G., Wong, J. P. S., Abbatt, J. P. D., Brune, W. H., Ng, N. L., Wright, J. P., Croasdale, D. R., Worsnop, D. R., Davidovits, P., and Onasch, T. B.: Characterization of aerosol photooxidation flow reactors: heterogeneous oxidation, secondary organic aerosol formation and cloud condensation nuclei activity measurements, Atmos. Meas. Tech., 4, 445-461, https://doi.org/10.5194/amt-4-445-2011, 2011.

Li, R., Palm, B. B., Ortega, A. M., Hlywiak, J., Hu, W. W., Peng, Z., Day, D. A., Knote, C., Brune, W. H., de Gouw, J. A.,
245       and Jimenez, J. L.: Modeling the radical chemistry in an oxidation flow reactor: radical formation and recycling, sensitivities, and the OH exposure estimation equation, J. Phys. Chem. A, 119, 4418-4432, https://doi.org/10.1021/jp509534k, 2015.

McMurry, P. H., and Grosjean, D.: Gas and aerosol wall losses in Teflon film smog chambers, Environ. Sci. Technol., 19, 1176-1182, https://doi.org/10.1021/es00142a006, 1985.

Mehra, A., Wang, Y., Krechmer, J. E., Lambe, A., Majluf, F., Morris, M. A., Priestley, M., Bannan, T. J., Bryant, D. J., Pereira,
250       K. L., Hamilton, J. F., Rickard, A. R., Newland, M. J., Stark, H., Croteau, P., Jayne, J. T., Worsnop, D. R., Canagaratna, M. R., Wang, L., and Coe, H.: Evaluation of the chemical composition of gas- and particle-phase products of aromatic oxidation, Atmos. Chem. Phys., 20, 9783-9803, https://doi.org/10.5194/acp-20-9783-2020, 2020.

Molteni, U., Bianchi, F., Klein, F., El Haddad, I., Frege, C., Rossi, M. J., Dommen, J., and Baltensperger, U.: Formation of highly oxygenated organic molecules from aromatic compounds, Atmos. Chem. Phys., 18, 1909-1921,
255       https://doi.org/10.5194/acp-18-1909-2018, 2018.

Orlando, J. J., Tyndall, G. S., and Wallington, T. J.: The atmospheric chemistry of alkoxy radicals, Chem. Rev., 103, 4657-4690, https://doi.org/10.1021/cr020527p, 2003.

Palm, B. B., Campuzano-Jost, P., Ortega, A. M., Day, D. A., Kaser, L., Jud, W., Karl, T., Hansel, A., Hunter, J. F., Cross, E. S., Kroll, J. H., Peng, Z., Brune, W. H., and Jimenez, J. L.: In situ secondary organic aerosol formation from ambient pine
260       forest air using an oxidation flow reactor, Atmos. Chem. Phys., 16, 2943-2970, https://doi.org/10.5194/acp-16-2943-2016, 2016.

Pan, S., and Wang, L.: Atmospheric oxidation mechanism of m-xylene initiated by OH radical, J. Phys. Chem. A, 118, 10778-10787, https://doi.org/10.1021/jp506815v, 2014.

Peng, Z., Day, D. A., Stark, H., Li, R., Lee-Taylor, J., Palm, B. B., Brune, W. H., and Jimenez, J. L.: HOx radical chemistry
265       in oxidation flow reactors with low-pressure mercury lamps systematically examined by modeling, Atmos. Meas. Tech., 8, 4863-4890, https://doi.org/10.5194/amt-8-4863-2015, 2015.

Peng, Z., and Jimenez, J. L.: Radical chemistry in oxidation flow reactors for atmospheric chemistry research, Chem. Soc. Rev., 49, 2570-2616, https://doi.org/10.1039/c9cs00766k, 2020.

Praske, E., Otkjær, R. V., Crounse, J. D., Hethcox, J. C., Stoltz, B. M., Kjaergaard, H. G., and Wennberg, P. O.: Atmospheric
270       autoxidation is increasingly important in urban and suburban North America, Proc. Natl. Acad. Sci. U. S. A., 115, 64-69, https://doi.org/10.1073/pnas.1715540115, 2018.

Schwantes, R. H., Schilling, K. A., McVay, R. C., Lignell, H., Coggon, M. M., Zhang, X., Wennberg, P. O., and Seinfeld, J.

H.: Formation of highly oxygenated low-volatility products from cresol oxidation, Atmos. Chem. Phys., 17, 3453-3474, https://doi.org/10.5194/acp-17-3453-2017, 2017.

275 Tsiligiannis, E., Hammes, J., Salvador, C. M., Mentel, T. F., and Hallquist, M.: Effect of NOx on 1,3,5-trimethylbenzene (TMB) oxidation product distribution and particle formation, Atmos. Chem. Phys., 19, 15073-15086, https://doi.org/10.5194/acp-19-15073-2019, 2019.

Wang, S., Wu, R., Berndt, T., Ehn, M., and Wang, L.: Formation of highly oxidized radicals and multifunctional products from the atmospheric oxidation of alkylbenzenes, Environ. Sci. Technol., 51, 8442-8449,
280 https://doi.org/10.1021/acs.est.7b02374, 2017.

Wu, R., Pan, S., Li, Y., and Wang, L.: Atmospheric oxidation mechanism of toluene, J. Phys. Chem. A, 118, 4533-4547, https://doi.org/10.1021/jp500077f, 2014.

Xu, C., and Wang, L.: Atmospheric oxidation mechanism of phenol initiated by OH radical, J. Phys. Chem. A, 117, 2358-2364, https://doi.org/10.1021/jp308856b, 2013.

285 Xu, L., Møller, K. H., Crounse, J. D., Kjaergaard, H. G., and Wennberg, P. O.: New insights into the radical chemistry and product distribution in the OH-initiated oxidation of benzene, Environ. Sci. Technol., 54, 13467-13477, https://doi.org/10.1021/acs.est.0c04780, 2020.

Zaytsev, A., Koss, A. R., Breitenlechner, M., Krechmer, J. E., Nihill, K. J., Lim, C. Y., Rowe, J. C., Cox, J. L., Moss, J., Roscioli, J. R., Canagaratna, M. R., Worsnop, D. R., Kroll, J. H., and Keutsch, F. N.: Mechanistic study of the formation of
290 ring-retaining and ring-opening products from the oxidation of aromatic compounds under urban atmospheric conditions, Atmos. Chem. Phys., 19, 15117-15129, https://doi.org/10.5194/acp-19-15117-2019, 2019.

Ziemann, P. J., and Atkinson, R.: Kinetics, products, and mechanisms of secondary organic aerosol formation, Chem. Soc. Rev., 41, 6582-6605, https://doi.org/10.1039/C2CS35122F, 2012.

295
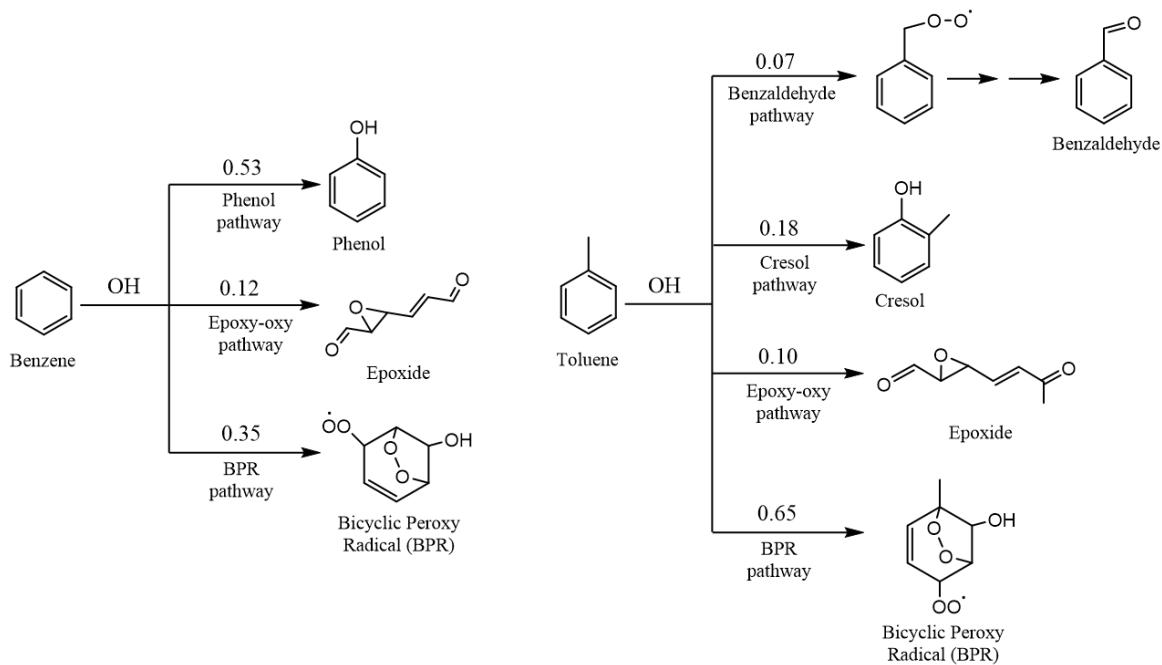
**Scheme S1.** Major gas-phase oxidation pathways for benzene and toluene in the MCM.

300
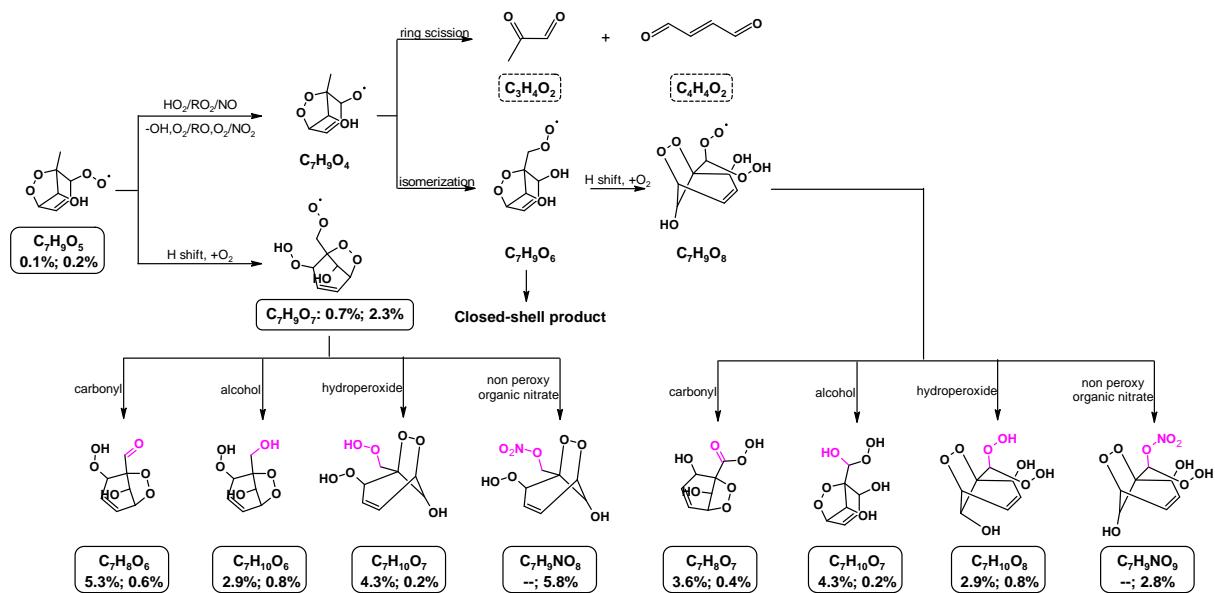
**Scheme S2.** A proposed mechanism involving the BPR $C_7H_9O_5$. The products shown in the box with dash and solid lines are measured by the PTR-QiTOF and the $NO_3^-$-TOF-CIMS, respectively. Numbers in the box represent the percentages of this molecule in total fitted ion signals for the OFR254-5 and OFR254-5-iN$_2$O4.4 experiments (Table S3). The functional groups shown in magenta represent the termination pathways.

305
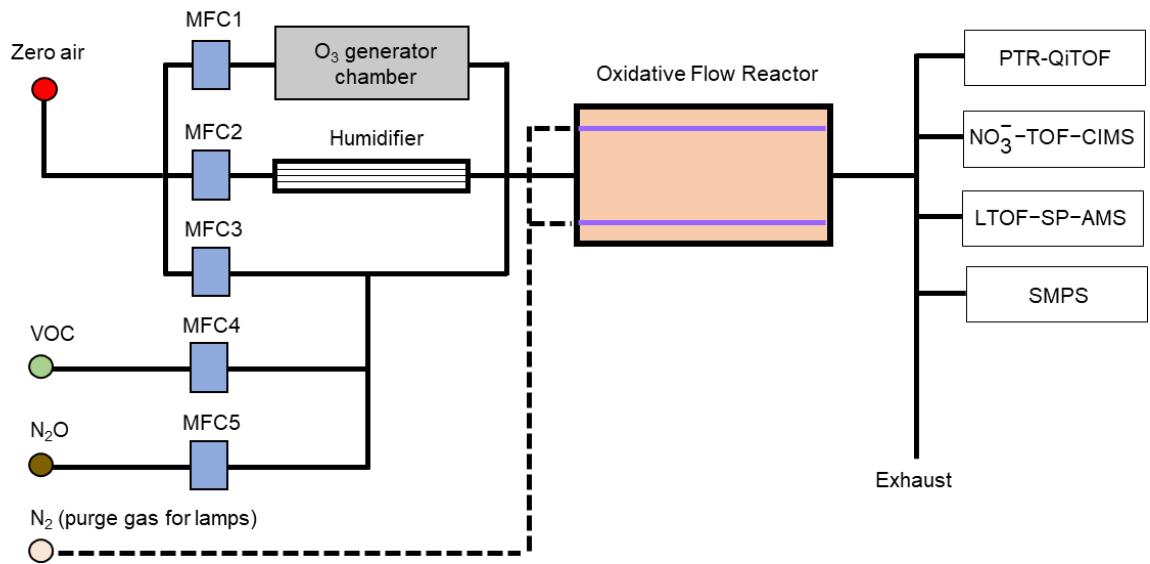
**Figure S1.** Schematic of the experimental setup of the benzene and toluene oxidation.

310
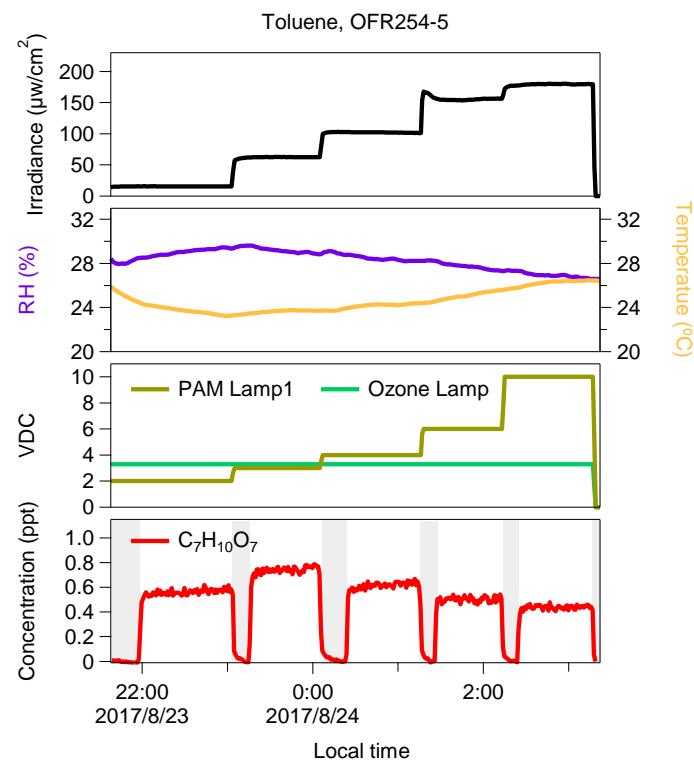
**Figure S2.** Time series of experimental conditions and an example HOM product for a typical OFR254-5 experiment of toluene oxidation under low-NOx conditions. The grey shaded area represent "background" periods without VOC injection.
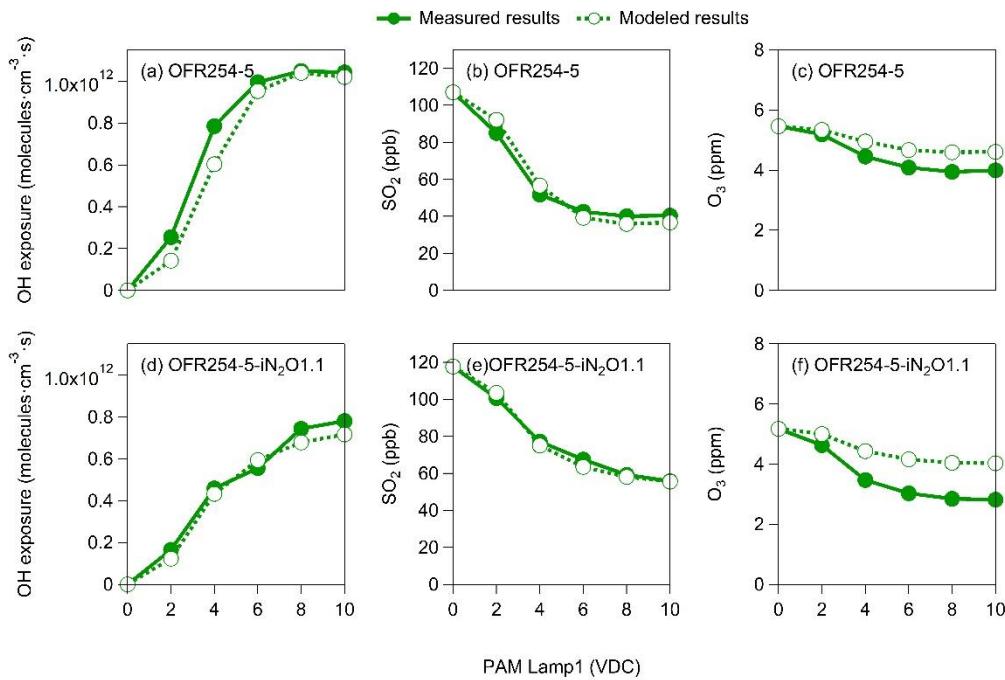
315

**Figure S3.** Measured and modeled results of OH exposure, $SO_2$ and $O_3$ concentrations for OFR254-5 and OFR254-5-iN$_2$O1.1 calibration experiments.
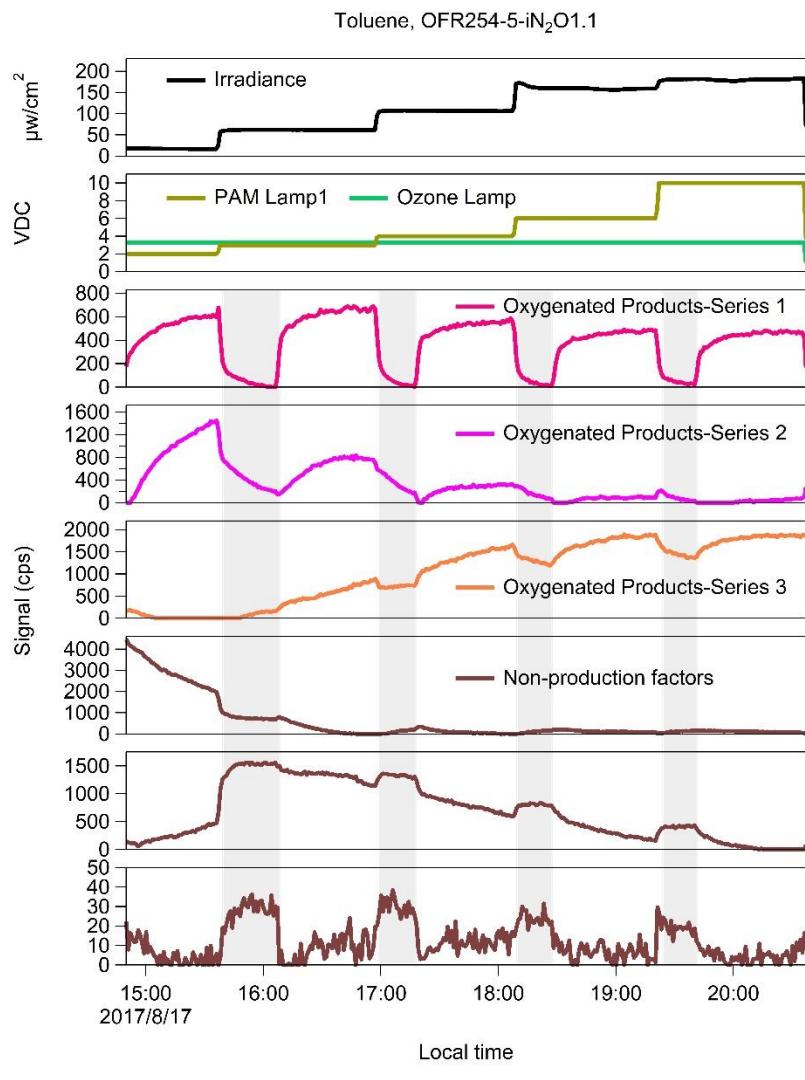
**Figure S4.** An example of PMF analysis for toluene oxidation under high-NO$_x$ conditions (OFR254-5-iN$_2$O1.1). The grey shaded areas represent "background" periods without VOC injection.
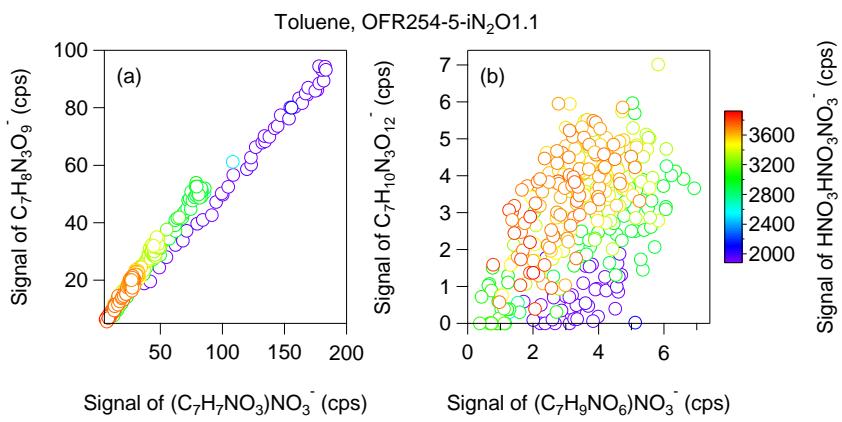
**Figure S5.** (a) A good correlation between the signals of $NO_3^-$-adduct ($C_7H_7NO_3$-$NO_3^-$) and $HNO_3NO_3^-$-adduct ($C_7H_7NO_3$-$HNO_3NO_3^-$) ions and (b) a poor correlation between the signals of $NO_3^-$-adduct ($C_7H_9NO_6$-$NO_3^-$) and $NO_3^-$-adduct ($C_7H_{10}N_2O_9$-$NO_3^-$) ions for an example toluene oxidation experiment under high-$NO_x$ (OFR254-5-iN$_2$O1.1) conditions.

325
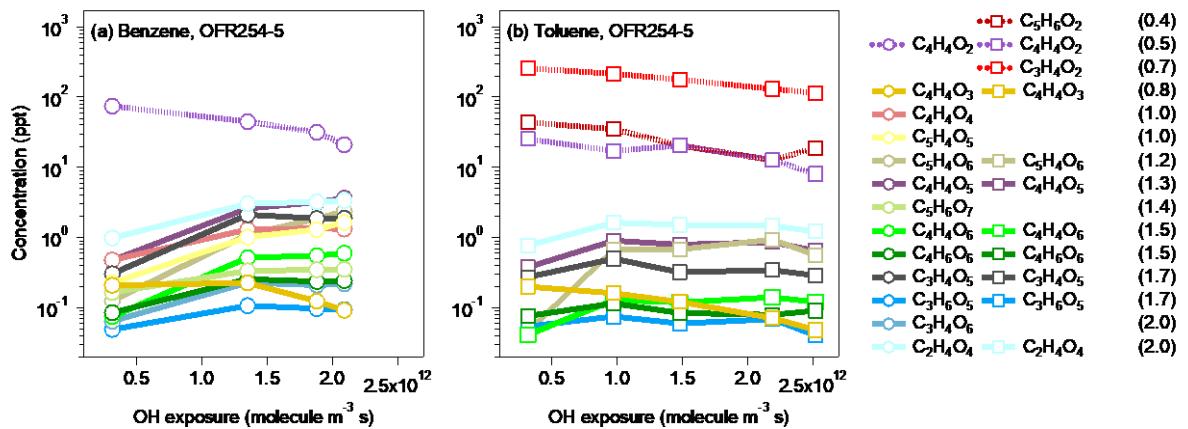
**Figure S6.** Concentrations of individual fragmented products as OH exposure increases under low-NO$_x$ (OFR254-5) conditions for benzene and toluene oxidation. The products shown in dash lines with symbols were quantified by the PTR-QiTOF, and the products shown in solid lines with symbols were quantified by the NO$_3^-$-TOF-CIMS. The numbers in parentheses refer to the O:C ratios of the molecules.
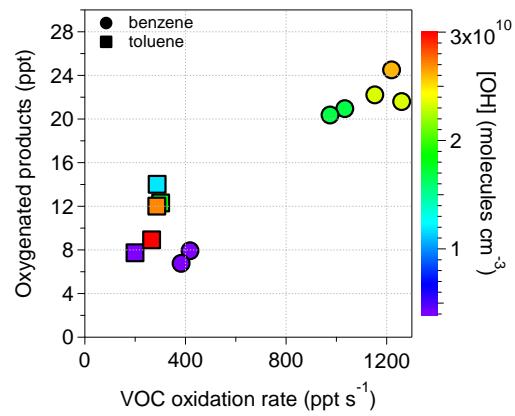
**Figure S7.** Scatter plot of the concentrations of total HOMs detected by the $NO_3^-$-TOF-CIMS and the VOC oxidation rates of benzene and toluene oxidation under low-NO$_x$ (OFR254-5) conditions.
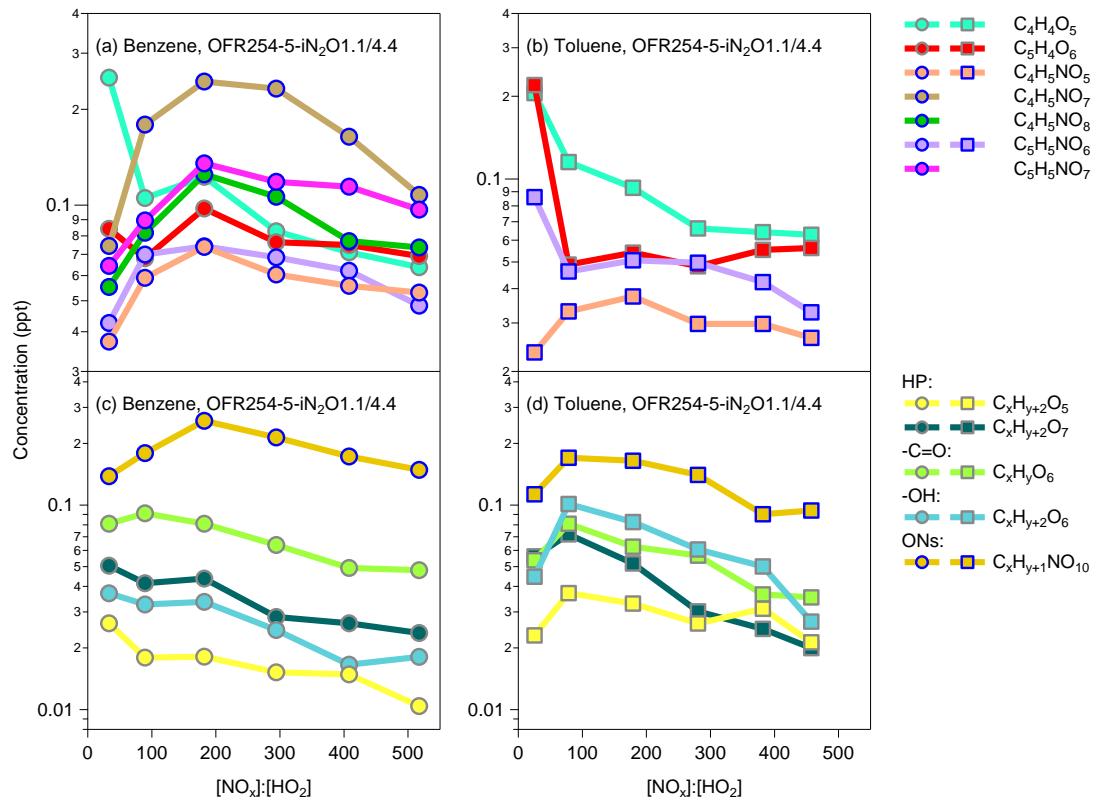
**Figure S8.** Concentrations of ring-scission and ring-retaining products measured by the $NO_3^-$-TOF-CIMS for increasing $[NO_x]$:$[HO_2]$ ratio for benzene and toluene oxidation under high-$NO_x$ conditions. HP: hydroperoxide; -C=O: carbonyl; -OH: alcohol; ONs: organic nitrates.

340

**Table S1.** Experimental conditions, measured and derived quantities in the OFR. The terms B and T represent benzene and toluene, respectively. Oxygenated products represent the sum of fragmented, closed-shell, open-shell, dimeric, and nitrogen-containing (if any) products measured by the $NO_3^-$-TOF-CIMS.

| Exp. No | VOC-Lamp voltage (V) | Experimental conditions | | | Measured quantities | | Derived quantities | | | |
|---|---|---|---|---|---|---|---|---|---|---|
| | | $N_2O_{in}$ (%, v/v) | RH (%) | Temperature (°C) | ΔVOC (ppb) | Oxygenated products (ppt) | $OH_{exp}$ (molec cm$^{-3}$ s) | $HO_2$ (ppb) | NO (ppb) | $NO_2$ (ppb) |
| 1* | B-2 | 0 | 23.6 | 25.0 | 32.3 | 6.8 | $3.1 \times 10^{11}$ | 1.5 | / | / |
| 2* | B-4 | 0 | 24.3 | 24.4 | 64.7 | 20.4 | $1.4 \times 10^{12}$ | 2.3 | / | / |
| 3* | B-6 | 0 | 24.0 | 25.0 | 72.2 | 22.2 | $1.9 \times 10^{12}$ | 2.4 | / | / |
| 4* | B-10 | 0 | 23.4 | 25.6 | 74.3 | 24.5 | $2.1 \times 10^{12}$ | 2.4 | / | / |
| 5* | B-2 | 1.1 | 25.3 | 22.9 | 20.2 | 18.6 | $1.1 \times 10^{11}$ | 0.8 | 0.2 | 17.4 |
| 6* | B-4 | 1.1 | 24.7 | 24.1 | 36.7 | 13.0 | $4.1 \times 10^{11}$ | 1.3 | 0.9 | 46.0 |
| 7* | B-6 | 1.1 | 23.6 | 25.8 | 41.9 | 9.9 | $5.8 \times 10^{11}$ | 1.4 | 1.4 | 49.9 |
| 8* | B-10 | 1.1 | 23.0 | 26.8 | 37.0 | 7.8 | $6.5 \times 10^{11}$ | 1.4 | 1.5 | 50.3 |
| 9# | B-2 | 4.4 | 49.7 | 23.8 | 27.4 | 17.9 | $1.4 \times 10^{11}$ | 0.7 | 0.6 | 60.5 |
| 10# | B-3 | 4.4 | 51.0 | 23.7 | 31.3 | 20.7 | $2.8 \times 10^{11}$ | 0.7 | 1.8 | 126.1 |
| 11# | B-4 | 4.4 | 48.5 | 24.7 | 33.8 | 15.0 | $3.7 \times 10^{11}$ | 0.6 | 3.2 | 176.1 |
| 12# | B-6 | 4.4 | 47.6 | 25.3 | 35.6 | 11.7 | $4.4 \times 10^{11}$ | 0.5 | 4.4 | 208.1 |
| 13# | B-10 | 4.4 | 46.0 | 25.7 | 36.3 | 9.9 | $4.6 \times 10^{11}$ | 0.5 | 5.1 | 231.4 |
| 14 | T-2 | 0 | 29.4 | 23.4 | 18.5 | 7.7 | $3.2 \times 10^{11}$ | 1.5 | / | / |
| 15 | T-3 | 0 | 29.0 | 23.7 | 25.8 | 14.0 | $9.8 \times 10^{11}$ | 2.2 | / | / |
| 16 | T-4 | 0 | 28.3 | 24.3 | 27.8 | 12.3 | $1.5 \times 10^{12}$ | 2.3 | / | / |
| 17 | T-6 | 0 | 27.5 | 25.4 | 29.4 | 12.0 | $2.2 \times 10^{12}$ | 2.3 | / | / |
| 18 | T-10 | 0 | 26.8 | 26.4 | 30.0 | 8.9 | $2.5 \times 10^{12}$ | 2.2 | / | / |
| 19 | T-2 | 1.1 | 27.2 | 25.1 | 22.1 | 8.0 | $1.4 \times 10^{11}$ | 0.9 | 0.2 | 15.8 |
| 20 | T-3 | 1.1 | 28.3 | 24.2 | 32.2 | 6.1 | $3.4 \times 10^{11}$ | 1.3 | 0.5 | 31.5 |
| 21 | T-4 | 1.1 | 27.8 | 24.9 | 35.6 | 4.6 | $5.0 \times 10^{11}$ | 1.4 | 0.9 | 37.5 |
| 22 | T-6 | 1.1 | 26.8 | 25.7 | 36.7 | 3.6 | $6.8 \times 10^{11}$ | 1.5 | 1.3 | 41.6 |
| 23 | T-10 | 1.1 | 26.2 | 26.1 | 36.5 | 3.3 | $7.4 \times 10^{11}$ | 1.5 | 1.5 | 43.1 |
| 24# | T-2 | 4.4 | 55.1 | 22.3 | 28.2 | 9.7 | $1.4 \times 10^{11}$ | 0.7 | 0.5 | 53.0 |
| 25# | T-3 | 4.4 | 54.5 | 22.7 | 30.3 | 10.3 | $2.9 \times 10^{11}$ | 0.7 | 1.9 | 123.2 |
| 26# | T-4 | 4.4 | 52.9 | 23.2 | 31.4 | 9.3 | $3.7 \times 10^{11}$ | 0.6 | 3.0 | 166.6 |
| 27# | T-6 | 4.4 | 51.7 | 23.8 | 32.2 | 8.0 | $4.3 \times 10^{11}$ | 0.5 | 4.1 | 196.3 |
| 28# | T-10 | 4.4 | 50.5 | 24.5 | 32.8 | 6.6 | $4.8 \times 10^{11}$ | 0.5 | 4.9 | 213.2 |

* Experiments that have repeated ones.

345  # Experiments that do not have PTR-QiTOF measurements.

**Table S2.** The peak list and relative signal contributions (%) of major gaseous products produced by the benzene oxidation experiments shown in Fig. 1a-b.

| Category | Formula | $m/z$ (Th) | Percentage in total fitted signal | | Listed by other studies of aromatic oxidation |
|---|---|---|---|---|---|
| | | | Exp. #2 (low $NO_x$) | Exp. #11 (high $NO_x$) | |
| Fragmented product | $C_2H_4O_4$ | 154.00 | 14.7% | 1.3% | |
| | $C_4H_4O_4$ | 178.00 | 6.2% | 1.6% | Mehra et al. (2020) |
| | $C_3H_4O_5$ | 181.99 | 9.9% | 0.2% | Mehra et al. (2020) |
| | $C_4H_2O_5$ | 191.98 | 2.1% | 3.5% | |
| | $C_4H_4O_5$ | 193.99 | 12.9% | 0.6% | Schwantes et al. (2017) Mehra et al. (2020) |
| | $C_4H_6O_5$ | 196.01 | 2.3% | 0.1% | Mehra et al. (2020) |
| | $C_5H_4O_5$ | 205.99 | 5.0% | 0.4% | Mehra et al. (2020) |
| | $C_5H_6O_5$ | 208.01 | 1.6% | 0.1% | Schwantes et al. (2017) Mehra et al. (2020) |
| | $C_4H_4O_6$ | 209.99 | 2.5% | 0.5% | Mehra et al. (2020) |
| | $C_4H_6O_6$ | 212.01 | 1.2% | 0.1% | Mehra et al. (2020) |
| | $C_5H_4O_6$ | 221.99 | 5.7% | 0.5% | Mehra et al. (2020) |
| | $C_5H_6O_7$ | 240.00 | 1.6% | 0.3% | Molteni et al. (2018) Garmash et al. (2020) |
| Closed-shell product | $C_6H_6O_4$ | 204.02 | 0.1% | / | Mehra et al. (2020) |
| | $C_6H_4O_5$ | 217.99 | 0.3% | 0.1% | Mehra et al. (2020) |
| | $C_6H_6O_5$ | 220.01 | 3.2% | 0.4% | Molteni et al. (2018) Mehra et al. (2020) |
| | $C_6H_8O_5$ | 222.03 | 0.4% | 0.01% | Molteni et al. (2018) Garmash et al. (2020) Mehra et al. (2020) |
| | $C_6H_4O_6$ | 233.99 | 0.7% | 0.2% | Mehra et al. (2020) |
| | $C_6H_6O_6$ | 236.01 | 3.0% | 0.4% | Molteni et al. (2018) Mehra et al. (2020) |
| | $C_6H_8O_6$ | 238.02 | 1.8% | 0.2% | Molteni et al. (2018) Mehra et al. (2020) |
| | $C_6H_{10}O_6$ | 240.04 | 0.1% | 0.04% | |
| | $C_6H_4O_7$ | 249.98 | 0.8% | 0.2% | |
| | $C_6H_6O_7$ | 252.00 | 2.6% | 0.3% | Molteni et al. (2018) Mehra et al. (2020) |
| | $C_6H_8O_7$ | 254.02 | 2.4% | 0.2% | Molteni et al. (2018) Garmash et al. (2020) |
| | $C_6H_{10}O_7$ | 256.03 | 0.5% | 0.03% | |
| | $C_6H_4O_8$ | 265.98 | 0.3% | 0.04% | |
| | $C_6H_6O_8$ | 268.00 | 1.3% | 0.4% | |
| | $C_6H_8O_8$ | 270.01 | 1.9% | 0.2% | Molteni et al. (2018) Garmash et al. (2020) |
| | $C_6H_{10}O_8$ | 272.03 | 0.8% | 0.1% | Molteni et al. (2018) |
| | $C_6H_6O_9$ | 283.99 | 0.6% | 0.04% | |
| | $C_6H_8O_9$ | 286.01 | 1.1% | 0.3% | Molteni et al. (2018) Garmash et al. (2020) |
| | $C_6H_{10}O_9$ | 288.02 | 0.4% | / | |
| | $C_6H_6O_{10}$ | 299.98 | 0.2% | 0.1% | |
| | $C_6H_8O_{10}$ | 302.00 | 0.4% | 0.1% | Molteni et al. (2018) |
| | $C_6H_{10}O_{10}$ | 304.02 | 0.2% | 0.1% | |
| Open-shell product | $C_6H_7O_5$ | 221.02 | 0.1% | 0.01% | Garmash et al. (2020) |
| | $C_6H_5O_6$ | 235.00 | 0.4% | 0.1% | |
| | $C_6H_5O_7$ | 250.99 | 0.8% | / | |
| | $C_6H_7O_7$ | 253.01 | 0.4% | 0.2% | Garmash et al. (2020) |
| | $C_6H_7O_9$ | 285.00 | 0.7% | 0.5% | Molteni et al. (2018) Garmash et al. (2020) |
| | $C_6H_7O_{10}$ | 300.99 | 0.5% | 0.2% | |
| Dimeric product | $C_{12}H_{14}O_8$ | 348.06 | 0.06% | / | Molteni et al. (2018) Garmash et al. (2020) |
| | $C_{12}H_{12}O_{10}$ | 378.03 | 0.14% | 0.04% | |
| | $C_{12}H_{14}O_{10}$ | 380.05 | 0.13% | 0.01% | Molteni et al. (2018) |

| | | | | | |
|---|---|---|---|---|---|
| | | | | | Garmash et al. (2020) |
| | $C_{12}H_{12}O_{11}$ | 394.03 | 0.10% | 0.01% | |
| | $C_{12}H_{14}O_{11}$ | 396.04 | 0.16% | / | Molteni et al. (2018) |
| | $C_{12}H_{14}O_{12}$ | 412.04 | 0.14% | 0.01% | Molteni et al. (2018) Garmash et al. (2020) |
| | $C_{12}H_{14}O_{13}$ | 428.03 | 0.14% | 0.02% | |
| | $C_{12}H_{14}O_{14}$ | 444.03 | 0.09% | / | Molteni et al. (2018) Garmash et al. (2020) |
| Nitrogen-containing product | $C_6H_5NO_3$ | 201.02 | / | 38.8% | Huang et al. (2014) |
| | $C_6H_5NO_4$ | 217.01 | / | 27.6% | Huang et al. (2014) |
| | $C_6H_4N_2O_6$ | 262.00 | / | 2.7% | Huang et al. (2014) |
| | $C_4H_5NO_5$ | 209.01 | / | 0.2% | |
| | $C_6H_7NO_5$ | 235.02 | / | 1.0% | |
| | $C_5H_5NO_6$ | 237.00 | / | 0.3% | |
| | $C_4H_5NO_7$ | 241.00 | / | 1.8% | |
| | $C_6H_5NO_6$ | 249.00 | / | 0.6% | |
| | $C_6H_7NO_6$ | 251.02 | / | 0.5% | |
| | $C_5H_5NO_7$ | 253.00 | / | 0.3% | |
| | $C_5H_7NO_7$ | 255.01 | / | 0.4% | |
| | $C_4H_5NO_8$ | 256.99 | / | 0.7% | |
| | $C_6H_7NO_7$ | 267.01 | / | 0.9% | |
| | $C_5H_5NO_8$ | 268.99 | / | 0.4% | |
| | $C_5H_7NO_8$ | 271.01 | / | 0.2% | |
| | $C_6H_5NO_8$ | 280.99 | / | 0.5% | |
| | $C_6H_7NO_8$ | 283.01 | / | 1.2% | |
| | $C_6H_9NO_8$ | 285.02 | / | 0.4% | |
| | $C_6H_7NO_9$ | 299.00 | / | 1.1% | |
| | $C_6H_9NO_9$ | 301.02 | / | 0.4% | |
| | $C_6H_8N_2O_9$ | 314.01 | / | 0.7% | |
| | $C_6H_7NO_{10}$ | 315.00 | / | 0.4% | |

**Table S3.** The peak list and relative signal contributions (%) of major gaseous products produced by the toluene oxidation experiments shown in Fig. 1c-d.

| Category | Formula | $m/z$ (Th) | Percentage in total fitted signal | | Listed by other studies of aromatic oxidation |
|---|---|---|---|---|---|
| | | | Exp. #16 (low NO$_x$) | Exp. #26 (high NO$_x$) | |
| Fragmented product | $C_2H_4O_4$ | 154.00 | 11.3% | 0.2% | |
| | $C_3H_4O_5$ | 181.99 | 3.0% | 0.2% | Mehra et al. (2020) |
| | $C_4H_2O_5$ | 191.98 | 0.7% | 5.7% | |
| | $C_4H_4O_5$ | 193.99 | 7.2% | 0.6% | Schwantes et al. (2017) Mehra et al. (2020) |
| | $C_4H_6O_5$ | 196.01 | 9.1% | 0.1% | Mehra et al. (2020) |
| | $C_4H_4O_6$ | 209.99 | 1.1% | 0.6% | Mehra et al. (2020) |
| | $C_5H_8O_5$ | 210.03 | 1.0% | 0.1% | Mehra et al. (2020) |
| | $C_5H_4O_6$ | 221.99 | 8.6% | 0.2% | Mehra et al. (2020) |
| Closed-shell product | $C_7H_8O_4$ | 218.03 | 0.3% | 0.3% | Schwantes et al. (2017) Molteni et al. (2018) Zaytsev et al. (2019) |
| | $C_7H_6O_5$ | 232.01 | 0.3% | 0.3% | Zaytsev et al. (2019) Mehra et al. (2020) |
| | $C_7H_8O_5$ | 234.03 | 1.5% | 0.4% | Schwantes et al. (2017) Molteni et al. (2018) Zaytsev et al. (2019) Mehra et al. (2020) |
| | $C_6H_6O_6$ | 236.01 | 5.0% | 0.2% | Molteni et al. (2018) Mehra et al. (2020) |
| | $C_7H_{10}O_5$ | 236.04 | 0.8% | 0.2% | Molteni et al. (2018) Zaytsev et al. (2019) Garmash et al. (2020) Mehra et al. (2020) |
| | $C_6H_8O_6$ | 238.02 | 2.0% | 0.4% | Molteni et al. (2018) Mehra et al. (2020) |
| | $C_7H_6O_6$ | 248.01 | 0.8% | / | Zaytsev et al. (2019) |
| | $C_7H_8O_6$ | 250.02 | 5.3% | 0.6% | Molteni et al. (2018) Zaytsev et al. (2019) Mehra et al. (2020) |
| | $C_6H_6O_7$ | 252.00 | 0.9% | 0.4% | Molteni et al. (2018) Mehra et al. (2020) |
| | $C_7H_{10}O_6$ | 252.04 | 2.9% | 0.8% | Molteni et al. (2018) Zaytsev et al. (2019) Mehra et al. (2020) |
| | $C_6H_8O_7$ | 254.02 | 1.6% | 0.7% | Molteni et al. (2018) Garmash et al. (2020) |
| | $C_7H_{12}O_6$ | 254.05 | 0.1% | 0.1% | Molteni et al. (2018) Mehra et al. (2020) |
| | $C_6H_{10}O_7$ | 256.03 | 0.4% | 0.1% | |
| | $C_7H_6O_7$ | 264.00 | 1.0% | / | |
| | $C_7H_8O_7$ | 266.02 | 3.6% | 0.4% | Mehra et al. (2020) |
| | $C_6H_6O_8$ | 268.00 | 0.2% | 0.1% | |
| | $C_7H_{10}O_7$ | 268.03 | 4.3% | 0.2% | Molteni et al. (2018) Mehra et al. (2020) |
| | $C_6H_8O_8$ | 270.01 | 0.6% | / | Molteni et al. (2018) Garmash et al. (2020) |
| | $C_7H_{12}O_7$ | 270.05 | 1.0% | 0.1% | Molteni et al. (2018) |
| | $C_7H_6O_8$ | 280.00 | 0.5% | 0.2% | |
| | $C_7H_8O_8$ | 282.01 | 2.3% | 0.4% | Molteni et al. (2018) |
| | $C_7H_{10}O_8$ | 284.03 | 2.9% | 0.8% | Molteni et al. (2018) |
| | $C_7H_{12}O_8$ | 286.04 | 1.5% | 0.2% | Molteni et al. (2018) |
| | $C_7H_8O_9$ | 298.01 | 0.3% | 0.5% | |
| | $C_7H_{10}O_9$ | 300.02 | 1.9% | 0.8% | Molteni et al. (2018) |
| | $C_7H_{12}O_9$ | 302.04 | 0.6% | / | |
| | $C_7H_8O_{10}$ | 314.00 | 0.4% | / | |
| | $C_7H_{10}O_{10}$ | 316.02 | 0.6% | 1.1% | Molteni et al. (2018) |

| | | | | | |
|---|---|---|---|---|---|
| | $C_7H_{12}O_{10}$ | 318.03 | 0.3% | / | |
| Open-shell product | $C_7H_9O_5$ | 235.03 | 0.1% | 0.2% | |
| | $C_7H_7O_6$ | 249.01 | 0.3% | 0.01% | |
| | $C_7H_7O_7$ | 265.01 | 0.2% | / | |
| | $C_7H_9O_7$ | 267.02 | 0.7% | 2.3% | |
| | $C_7H_9O_9$ | 299.01 | 1.5% | 1.2% | Molteni et al. (2018) |
| | $C_7H_9O_{10}$ | 315.01 | 0.6% | 0.1% | |
| Dimeric product | $C_{14}H_{18}O_8$ | 376.09 | 0.06% | / | Molteni et al. (2018) Garmash et al. (2020) |
| | $C_{14}H_{18}O_{10}$ | 408.08 | 0.15% | 0.02% | Molteni et al. (2018) |
| | $C_{14}H_{16}O_{11}$ | 422.06 | 0.11% | 0.07% | |
| | $C_{14}H_{18}O_{11}$ | 424.07 | 0.12% | 0.02% | Molteni et al. (2018) |
| | $C_{14}H_{20}O_{11}$ | 426.09 | 0.15% | 0.00% | Molteni et al. (2018) |
| | $C_{14}H_{16}O_{12}$ | 438.05 | 0.11% | 0.14% | |
| | $C_{14}H_{18}O_{12}$ | 440.07 | 0.18% | 0.07% | Molteni et al. (2018) |
| | $C_{14}H_{20}O_{12}$ | 442.08 | 0.08% | / | |
| | $C_{14}H_{18}O_{14}$ | 472.06 | 0.11% | / | Molteni et al. (2018) |
| Nitrogen-containing product | $C_6H_5NO_3$ | 201.02 | / | 15.6% | Huang et al. (2014) |
| | $C_7H_7NO_3$ | 215.03 | / | 8.7% | |
| | $C_6H_5NO_4$ | 217.01 | / | 4.4% | Huang et al. (2014) |
| | $C_7H_7NO_4$ | 231.03 | / | 2.4% | |
| | $C_6H_4N_2O_6$ | 262.00 | / | 0.3% | Huang et al. (2014) |
| | $C_4H_5NO_5$ | 209.01 | / | 0.2% | |
| | $C_7H_5NO_4$ | 229.01 | / | 1.1% | Zaytsev et al. (2019) |
| | $C_5H_5NO_6$ | 237.00 | / | 0.4% | |
| | $C_7H_9NO_5$ | 249.04 | / | 1.0% | Zaytsev et al. (2019) |
| | $C_5H_5NO_7$ | 253.00 | / | 0.7% | |
| | $C_6H_9NO_6$ | 253.03 | / | 0.7% | |
| | $C_5H_7NO_7$ | 255.01 | / | 2.1% | |
| | $C_7H_7NO_6$ | 263.02 | / | 0.9% | Zaytsev et al. (2019) |
| | $C_7H_9NO_6$ | 265.03 | / | 2.0% | Zaytsev et al. (2019) |
| | $C_6H_8N_2O_6$ | 266.03 | / | 0.6% | |
| | $C_6H_7NO_7$ | 267.01 | / | 0.6% | |
| | $C_6H_9NO_7$ | 269.03 | / | 1.1% | Tsiligiannis et al. (2019) |
| | $C_5H_7NO_8$ | 271.01 | / | 1.4% | |
| | $C_7H_9NO_7$ | 281.03 | / | 3.4% | Zaytsev et al. (2019) |
| | $C_6H_9NO_8$ | 285.02 | / | 1.4% | |
| | $C_7H_7NO_8$ | 295.01 | / | 0.7% | |
| | $C_7H_9NO_8$ | 297.02 | / | 5.8% | Zaytsev et al. (2019) |
| | $C_7H_7NO_9$ | 311.00 | / | 0.6% | |
| | $C_7H_9NO_9$ | 313.02 | / | 2.8% | |
| | $C_6H_8N_2O_9$ | 314.01 | / | 0.5% | |
| | $C_7H_{11}NO_9$ | 315.03 | / | 2.0% | |
| | $C_7H_{10}N_2O_9$ | 328.03 | / | 1.0% | |
| | $C_7H_9NO_{10}$ | 329.01 | / | 1.7% | |

**Table S4.** Experimental conditions and gaseous oxygenated products for the photooxidation of benzene in previous studies and this study. We normalize the abundance of all listed ions to that of $C_6H_7O_9$ which is a commonly observed $RO_2$ radical for comparison.

| Conditions and Products | Molteni et al. (2018) Flow tube | Garmash et al. (2020) Flow tube | Garmash et al. (2020) JPAC | This study OFR (Exp. #2) |
|---|---|---|---|---|
| Experimental conditions | | | | |
| Residence time | 20 s | 10 s | 48 min | 95 s |
| [Benzene] (molecules cm$^{-3}$) | $9.85 \times 10^{13}$ | $\sim 1.00 \times 10^{16}$ | $7.22 \times 10^{10}$ | $2.72 \times 10^{12}$ |
| [OH] (molecules cm$^{-3}$) | $8.50 \times 10^{11}$ | N/A | $4.46 \times 10^8$ | $1.67 \times 10^{10}$ |
| [Benzene]:[OH] | 116 | N/A | 162 | 163 |
| Relative proportion of oxygenated products (normalize to the signal of $C_6H_7O_9$) | | | | |
| $C_6H_7O_5$ | / | 0.02 | / | 0.14 |
| $C_6H_7O_7$ | / | 0.05 | / | 0.57 |
| $C_6H_7O_9$ | 1 | 1 | 1 | 1 |
| $C_6H_8O_5$ | 12.82 | 1.09 | / | 0.57 |
| $C_6H_8O_7$ | 1.55 | 0.35 | 3.99 | 3.43 |
| $C_6H_8O_9$ | 2.36 | 1.70 | 3.48 | 1.57 |
| $C_{12}H_{14}O_8$ | 5.55 | 1.73 | 0.29 | 0.09 |
| $C_{12}H_{14}O_{10}$ | 0.64 | 0.48 | 0.55 | 0.19 |
| $C_{12}H_{14}O_{12}$ | 1.18 | 1.27 | 0.57 | 0.20 |
| $C_{12}H_{14}O_{14}$ | 1.64 | 0.32 | 0.38 | 0.13 |